



# Deformation Behavior and Cavitation of AA2017 at Elevated Temperatures

E. Vaghefi<sup>1</sup> · S. Serajzadeh<sup>1</sup>

Received: 11 February 2020 / Accepted: 28 April 2020 / Published online: 29 May 2020  
© The Korean Institute of Metals and Materials 2020

## Abstract

In this work, deformation behavior of AA2017-T4 at elevated temperatures was studied employing uni-axial tensile and creep experiments. Tensile tests were carried out at temperatures varying 150–500 °C under different strain rates then, a combination of neural network and dynamic material modeling was utilized to construct the processing maps. Furthermore, creep experiments were conducted to assess inelastic deformation behavior of the alloy at temperatures between 150 and 225 °C and stresses in the range of 150 to 230 MPa. Microstructural evaluations were carried out for determination of microstructural changes and formation of voids and cavities within the samples. The results showed that dynamic precipitation could occur during deformation at temperatures 175–225 °C leading to negative strain-rate sensitivity at true strains larger than 0.1. The main softening process was detected as dynamic recovery at temperatures higher than 250 °C however, dynamic recrystallization could also occur at low strain rates and temperatures higher than 400 °C. The activation energies for hot deformation were computed as 380.6 kJ mole<sup>-1</sup> at 250–350 °C and it was reduced to 224.7 kJ mole<sup>-1</sup> for the range of 350–500 °C. This showed the hard particle could significantly change rate of flow softening. The creep activation energy was determined as 169.5 kJ while the stress-exponent varied between 5.5 and 10.1 at temperatures between 150 and 225 °C indicating that dynamic recovery controlled by dislocation climb could be the governing creep mechanism.

**Keywords** Aluminum–copper alloy · Creep · Hot deformation · Cavitation · Dynamic precipitation

## 1 Introduction

Aluminum alloys are used in various industrial applications owing to their high yield stress/weight and corrosion resistance while one of the significant task in application and/or manufacturing of these materials is their mechanical behavior at elevated temperatures. Various investigations were carried out to determine high temperature behavior of these alloys considering different aspects such as softening mechanisms, creep rate and creep rupture, and dynamic precipitation. For instance; Carmona et al. [1] studied thermo-mechanical processing of an Al–Mg alloy under warm working conditions using uni-axial tensile and compression tests. It was found that the mechanisms of dislocation climb and solute drag might be operative during warm deformation.

Cepeda-Jiménez et al. [2] investigated deformation behavior and softening mechanisms in AA2024 alloy by means of torsion tests in the range of 278–476 °C under applied strain rates of 2.1 s<sup>-1</sup> and 25.6 s<sup>-1</sup>. Nayan et al. [3] studied microstructural events within AA 2195 during plane-strain compression at high temperatures in the range of 300–450 °C and strain rates of 0.01–1 s<sup>-1</sup> in which it was found that dynamic recrystallization could occur under low strain rates. Fan et al. [4] examined hot deformation behavior of Al–Mg–Si alloy through compression testing under strain rates of 0.01, 0.1 and 1 s<sup>-1</sup> and temperatures of 400 °C, 450 °C and 500 °C together with microstructural evolutions. Dynamic recovery (DRV) was found to be the dominant softening mechanisms however, at temperature higher than 400 °C and low strain rates, dynamic recrystallization was also observed. Cavaliere [5] studied hot and warm formability of AA2618 employing torsion testing where it was shown that dynamic precipitation processes could take place during deformation leading to significant microstructural changes. Serajzadeh et al. [6] studied on flow stress behavior of AA2017–SiCp by uni-axial compression test at warm and hot deformation

✉ S. Serajzadeh  
serajzadeh@sharif.edu

<sup>1</sup> Department of Materials Science and Engineering, Sharif University of Technology, Tehran, P.O. Box 11365-9466, 1458889694, Iran

temperatures. Spigarelli et al. [7] investigated hot formability of AA2014 alloy in a wide range of temperatures and strain rates using torsion tests and then, an appropriate constitutive equation was derived for describing the dependence of flow stress, deformation temperature and applied strain rate. Huang et al. [8] defined the flow stress behavior of Al–4.39Cu–1.15Mg–0.51Mn–0.12Zr alloy during hot compression utilizing Zener–Hollomon parameter. It was observed that at low  $Z$ -values, coarse precipitates were distributed within microstructure however, deformation under high- $Z$  levels was led to formation of fine precipitates. Li et al. [9] investigated the hot deformation behavior and processing maps of AA2519 using isothermal compression testing in the temperatures ranging from 300 to 450 °C at strain rates of 0.01–10 s<sup>-1</sup>. Jin et al. [10] investigated the high-temperature deformation behavior, flow localization and processing maps of AA7050 utilizing tensile tests conducted at various temperatures and strain rates. Xu et al. [11] studied creep deformation of AA2124 under different stress levels and temperatures. Based on the achieved experimental data, the creep constitutive equations were proposed for the case of the examined alloy. Yang et al. [12] studied deformation processes and concurrent precipitation during creep-aging of AA2124-T851. They demonstrated that the mean length of strengthening precipitates increases gradually during creep-aging while the main strengthening particles were identified as Al<sub>2</sub>CuMg or Al<sub>2</sub>Cu. Du et al. [13] studied creep-aging of a hardenable aluminum alloy i.e. AA2618, during stress-controlled creep experiments at temperatures ranging between of 180 and 240 °C. Lin et al. [14] investigated the effects of the external stress and creep aging temperature on the hardness and precipitates of 2024-T3 aluminum alloy at different temperatures and stresses in which it was found that precipitating process is more sensitive to temperature than applied stress. In the other work, Majimel et al. [15] investigated precipitation and coarsening of particles during creep-aging of AA2650-T8 alloy. They suggested that the diffusion through dislocation cores could be responsible for coarsening of particles.

Regarding the published works, it can be noted that heat-treatable aluminum alloys show a sophisticated mechanical behavior at high temperature owing to the occurrence of different phenomena such as dynamic softening processes, precipitation and formation of cavities. In this regard, in this work, high-temperature deformation and creep behavior of a heat-treatable aluminum alloy i.e. AA2017-T4, was examined employing uni-axial tensile testing together with stress-controlled creep experiments. The tensile testing was conducted on flat samples at temperatures varying between 150 and 500 °C and strain rates of 0.0005, 0.002, 0.005, 0.02, 0.05 (s<sup>-1</sup>). The creep experiments were also carried out at temperatures between 150 and 225 °C under applied stresses of 150, 180, 210, and 230 (MPa). Microstructural evolutions

were then performed by means of optical metallography and scanning electron microscopy in order to study microstructural events and formation and growth of cavities during creep deformation. Finally, the governing deformation and restoration mechanisms, processing maps and cavitation mechanisms were determined and justified.

## 2 Materials and Experiments

An aluminum-copper alloy, AA2017, was examined in this work. The chemical composition of the alloy was 4.18% Cu, 0.51% Mg, 0.68% Si, 0.79% Mn, 0.25% Fe and balanced Al (in wt%). The as-received plate with the thickness of 9 mm was first subjected to multi-pass hot rolling operation to reduce the thickness to about 2.8 mm then, solution treatment was performed at 500 °C for 1 h and after that, the alloy was quenched in water and natural aging was allowed to be occurred. In order to obtain a proper aging period, the changes in the hardness were measured employing Vickers hardness technique using 10 kgf. The recorded hardness vs. time diagram is shown in Fig. 1. As seen the hardness reached a constant value after about 14 days and accordingly, the duration of natural aging was taken at least 14 days.

The uni-axial creep experiments were then performed on the naturally-aged samples at different temperatures including 150 °C, 175 °C, 200 °C, and 225 °C while the applied stresses were 150 MPa, 180 MPa, 210 MPa, and 230 MPa. In creep testing, the samples were first heated to the test temperature within 25 min. and then, they were held for 30 min under isothermal conditions to obtain a uniform temperature

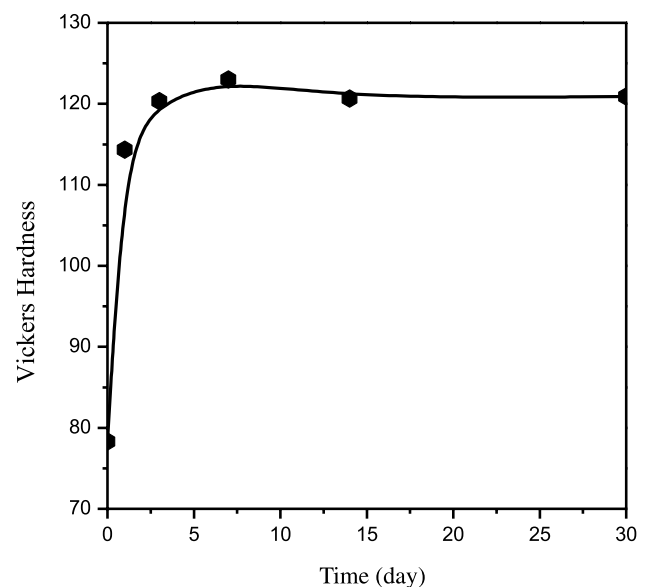


**Fig. 1** Variations Vickers hardness during natural aging of the examined alloy

distribution. In fact a similar heating time including heating stage and holding time were employed for all samples regarding the possible precipitation during heating stage. Besides, uni-axial tensile testing was made for determination of deformation behavior of the alloy. Note that the size of the tensile and creep samples was 32 mm × 6 mm × 2.8 mm according to ASTM-E8M and ASTM E139. The tests were conducted at room temperature, 150 °C, 175 °C, 200 °C, 250 °C, 300 °C, 350 °C, 400 °C, 450 °C and 500 °C. The samples were heated to the deformation temperature and then held for 3 min. to achieve uniform temperature distribution along gage-length and then deformation was applied under relatively low strain rates of 0.0005 s<sup>-1</sup>, 0.002 s<sup>-1</sup>, 0.005 s<sup>-1</sup>, 0.02 s<sup>-1</sup>, and 0.05 s<sup>-1</sup>. This made it possible to investigate the occurrence of dynamic precipitation and/or dynamic recrystallization that might be activated at low deformation rates. It should be mentioned that three main strain rates including 0.05 s<sup>-1</sup>, 0.005 s<sup>-1</sup>, and 0.0005 s<sup>-1</sup> were applied for all temperatures. Afterwards, in order to a better understanding of metallurgical phenomena, additional strain rates were also considered and tested based on the flow stress behavior of the alloy. For instance, dynamic precipitation was detected during deformation at low temperatures e.g. 150 and 200 °C under low strain rate. Accordingly, additional strain rate i.e. 0.002 s<sup>-1</sup> was also taken into account.

After deformation, the specimens were rapidly cooled to room temperature to capture the as-deformed microstructures and microstructural observation was then carried out on the samples. The upper sides of the deformed samples were considered in the microstructural experiments. The optical metallography was conducted utilizing polishing and chemical etching technique employing the etchant made of 2 ml HF, 20 ml HNO<sub>3</sub>, 3 ml HCL and 175 ml water. Scanning electron microscopy (SEM) was also conducted to study the formation and growth of the cavities after creep deformation. It should be noted that software Image J was utilized for determination of mean grain size and fraction of cavitations within the deformed alloy.

In the next stage, processing maps were constructed for prediction of the dynamic responses of the alloy and determination of deformation efficiency. In order to construct these maps, it was required to determine flow stress behavior of the examined material under various conditions. Accordingly, an artificial neural network (ANN) was first developed to define flow stress at different temperatures, strain and strain rate employing the results of the tensile tests. A typical ANN architecture included the input, output, and hidden layers were connected via neurons as processing units. The main idea was to minimize the errors between the ANN

outputs and the experimental values. The back-propagation algorithm was utilized to train the network while hyperbolic tangent, sigmoid, and linear functions were employed for relating the hidden layers and output layer, respectively [16]. The output layer contained flow stress and input layer consisted of three levels including temperature, strain rate and strain that were first normalized in the range of -1 to +1 to ensure all inputs had the same impact. Then, 70% of the data was randomly selected to train the network and the other 30% was employed to test and to validate the output of the constructed ANN. The network convergence criterion was established by the mean square error (MSE) between the desired and estimated output values as expressed by Eq. 1 and the convergence criterion of 0.015 was set in all calculations [17].

$$MSE = \frac{1}{N} \sum_{i=1}^N (E_i - P_i)^2 \quad (1)$$

here,  $E_i$  and  $P_i$  are the experimental and estimated values.  $N$  denotes the total number of training data. Note that the following correlation coefficient was used for performance evaluation of the network [18].

$$R = \frac{\sum_{i=1}^N (E_i - \bar{E})(P_i - \bar{P})}{\sqrt{\sum_{i=1}^N (E_i - \bar{E})^2 \sum_{i=1}^N (P_i - \bar{P})^2}} \quad (2)$$

in the above equation,  $\bar{E}$  and  $\bar{P}$  are the mean values of parameters  $E_i$  and  $P_i$ , respectively. After training a proper network with the desired precision, the results of ANN modeling were considered for prediction of the flow stress behavior of the alloy and construction of the processing maps. To do so, the diagrams of  $\ln(\sigma)$  vs.  $\ln(\dot{\epsilon})$  were defined based on the predicted diagrams by the ANN model with high precision. Afterwards, the strain rate sensitivity parameter were computed under small increments of temperatures and strain rates. In this regard, the temperature interval was selected as 10 °C and the strain rate increment was taken 0.0001 s<sup>-1</sup>. The strain rate sensitivity was calculated using the following equation.

$$m = \frac{d \ln(\bar{\sigma})}{d \ln(\dot{\epsilon})} = \frac{\dot{\epsilon} d\bar{\sigma}}{\bar{\sigma} d\dot{\epsilon}} \quad (3)$$

In the next step, the processing maps were developed employing dynamic material modeling in a temperature-strain rate space [18]. The total volumetric power can be described by superposition of the power dissipated by plastic

deformation together with the associated power related to occurrence of metallurgical events like dynamic recovery and recrystallization i.e. complementary power dissipation. This can be mathematically described as follows [10]

$$P = G + J = \int \bar{\sigma} d\bar{\epsilon} + \int \dot{\bar{\epsilon}} d\bar{\sigma} \tag{4}$$

here,  $P$  denotes the total power dissipation,  $G$  and  $J$  are plastic work dissipation and complementary dissipation power, respectively. Utilizing the calculated strain rate sensitivity and power-law constitutive equation, the J-parameter can be defined as:

$$J = \int \dot{\bar{\epsilon}} d\bar{\sigma} = \int m \bar{\sigma} d\bar{\epsilon} = \frac{m \bar{\sigma} \bar{\epsilon}}{m + 1} \tag{5}$$

Note that the maximum value of  $J$  can be calculated as  $\frac{\bar{\sigma} \bar{\epsilon}}{2}$  when the strain rate sensitivity reaches  $m = 1$ . Accordingly, the efficiency of power dissipation can be determined as follows.

$$\eta = \frac{J}{J_{\max}} = \frac{2m}{m + 1} \tag{6}$$

It should be noted that during deformation, the regions having the maximum efficiency are of interest. However, microstructural instabilities might be operative while these phenomena was determined by mapping the instability parameter according to the following inequality [18]:

$$\xi(\dot{\bar{\epsilon}}) = \frac{\partial \ln(m/m + 1)}{\partial \ln \dot{\bar{\epsilon}}} + m \leq 0 \tag{7}$$

The domain with the negative value of parameter- $\xi$ , might be considered as the region associated with microstructural instability. Finally, the processing map was constructed by combination of instability map together with map of the power dissipation. Figure 2 shows the procedure used to construct the processing maps.

### 3 Results and Discussion

The microstructure of the naturally aged sample and corresponding stress–strain diagram are given in Fig. 3. It can be seen that the microstructure shows a uniform and equiaxed grain structure having the mean grain size of about 93  $\mu\text{m}$ . Figure 3b shows the stress–strain diagrams at room temperature after different aging times. The serrated flow can be distinguished for the as-quenched sample however, the serrations were suppressed after 14 days natural aging. It demonstrates that precipitation during aging decreases solute atoms that are responsible for the occurrence of serrated yielding [19]. Figure 4 displays the stress–strain diagrams

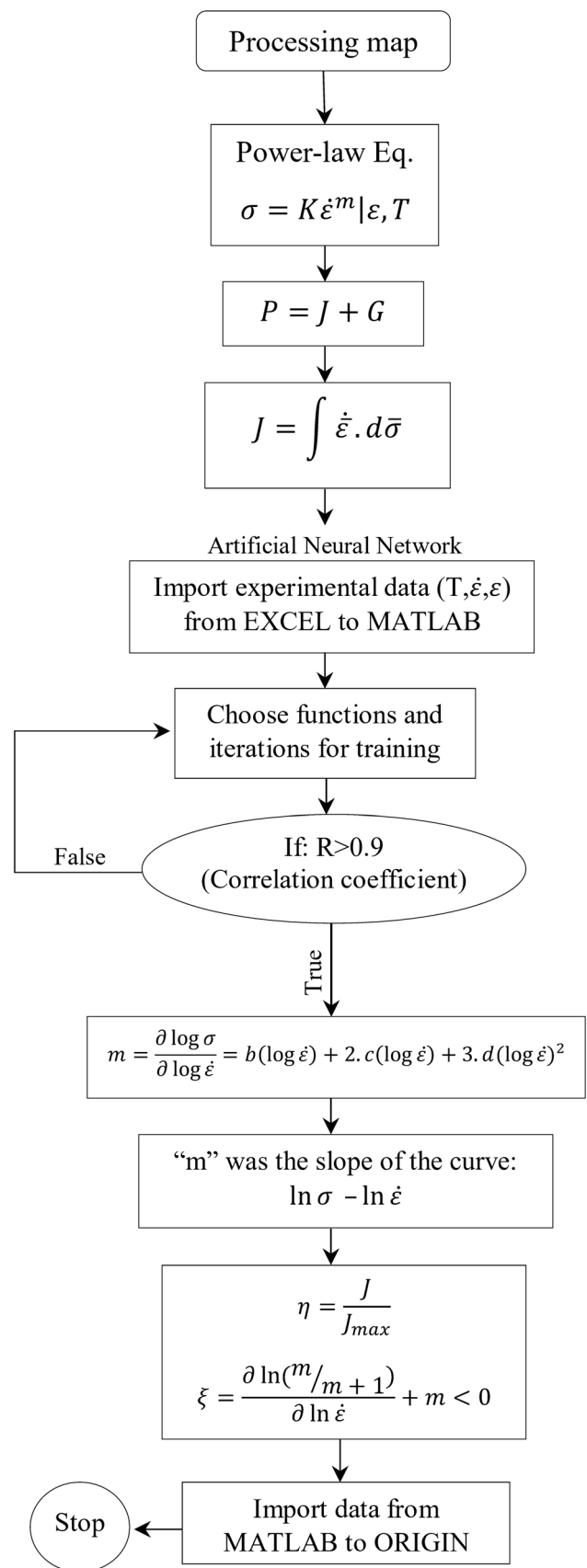
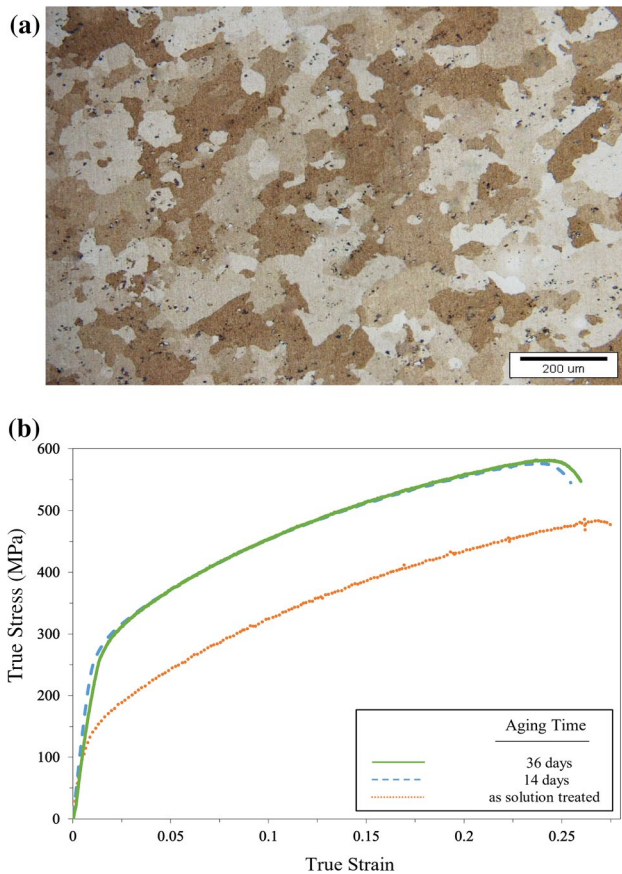


Fig. 2 The steps used for determination of deformation processing maps





**Fig. 3** **a** Microstructure of the naturally aged alloy, **b** stress–strain diagrams of as-solution treated and aged alloy

of the aged-alloy at different temperatures and strain rates and Fig. 5 demonstrates variation of the calculated mean strain-rate sensitivity parameter vs. temperature at true strain of 0.1. Note that the strain rate sensitivity parameter was computed based on the experimental data and Eq. 3 i.e. the slope of the best line in  $\ln(\sigma)$  vs.  $\ln(\dot{\epsilon})$  coordinate. It is worth noting that different hardening/softening phenomena are operative given the applied strain-rate and temperature. Dynamic precipitation at low temperatures i.e. at 200 °C or less, can be detected from the stress–strain diagrams leading to negative strain rate sensitivity [5]. On the other hand, regular behavior can be observed at temperatures higher than 225 °C during which the alloy exhibits positive strain rate sensitivity while the amount of strain hardening significantly decreases at temperatures higher than 250 °C. Regarding the flow stress diagrams, the governing dynamic softening is attributed to dynamic recovery [8]. Note that at low temperatures the amount of recovery is small and hence the effect of strain-rate is trivial. However, at temperatures higher than

$0.6T_{mp}$  i.e. 230 °C or above, the diffusion rate as well as dislocation reactions would be made more rapidly which in turn it results in higher rate of dynamic softening as well as higher strain rate sensitivity [20].

Regarding the high stacking fault energy of aluminum alloys, dynamic recovery can be considered as the main softening mechanism. According to Fig. 4, the typical dynamic recovery behavior can be detected particularly at high strain rates. Figure 6 displays optical micrographs of the examined alloy after hot deformation under different temperatures and strain rates. It is observed that different microstructures were produced after hot deformation in which the average grain size was reduced to about 41  $\mu\text{m}$  after deformation at 500 °C and strain rate of  $0.005 \text{ s}^{-1}$  however, the mean grain diameter was about 85  $\mu\text{m}$  after deformation at 400 °C and strain rate of  $0.02 \text{ s}^{-1}$ . Regarding Fig. 6a, the elongated grains can be distinguished while the mean grain size was not significantly altered as compared with the as-annealed condition displayed in Fig. 3a. Note that the deformed microstructure could be consist of equiaxed grains and/or elongating grains in which the dynamic recrystallization is responsible for formation of fine-equiaxed grain structure while the elongated grain structure indicates the occurrence of dynamic recovery [21]. Figure 6b and Fig. 7 clearly demonstrates the formation of fine and equiaxed grain within microstructure i.e. a bimodal structure. Furthermore, Fig. 8 displays the grain size distribution within the sample deformed at 500 °C and strain rate of  $0.005 \text{ s}^{-1}$ . There is a relatively wide distribution of grain size in this sample. Thus, it can be concluded that the dynamic recrystallization occurred at high temperatures and low strain rates. Moreover, it may be stated that the discontinuous dynamic recrystallization associated with nucleation and growth the nucleation is the governing mechanism.

The governing constitutive equation under hot deformation conditions can be expressed by hyperbolic-sine function as follows [2].

$$Z = \dot{\epsilon} \exp\left(\frac{Q}{RT}\right) = A[\sinh(\alpha\sigma_{ss})]^n \quad (8)$$

here,  $A$  and  $n$  are material constants,  $Z$  denotes the Zener–Hollomon parameter,  $Q$  is the apparent activation energy, and  $R$  is the gas constant. In order to define the material parameters, the natural logarithm was first taken from the above equation as below.

$$\ln(Z) = \ln(A) + n \ln((\sinh(\alpha\sigma_{ss}))^n) \quad (9)$$

Then, a trial and error procedure was utilized for determination of stress multiplier i.e.  $\alpha$ -parameter. In this scheme, various values of  $\alpha$ -parameter were examined and the

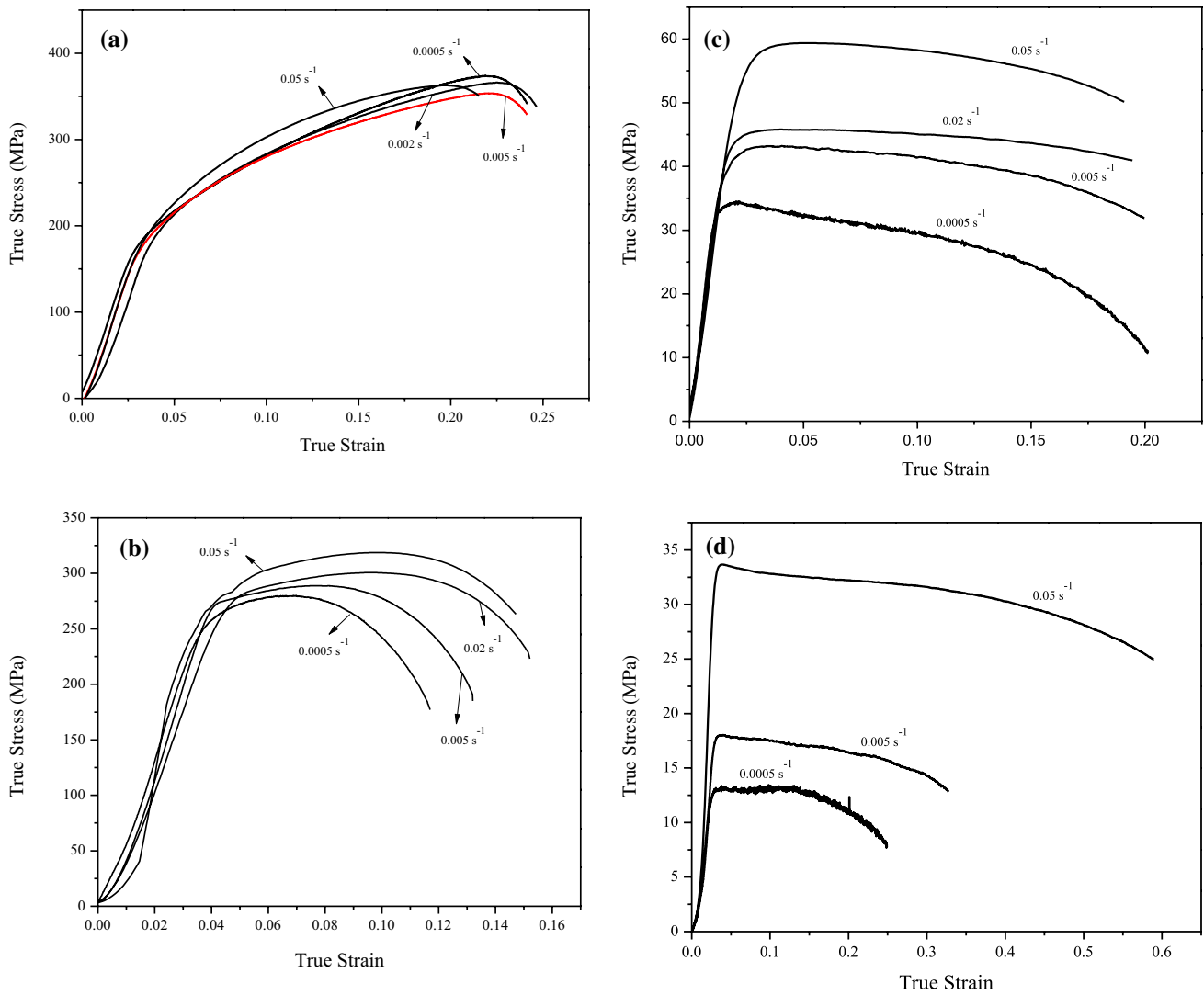


**Fig. 4** Stress–strain diagrams of AA2017-T4 under different strain rates, **a** at 200 °C, **b** at 250 °C, **c** at 400 °C, **d** at 500 °C

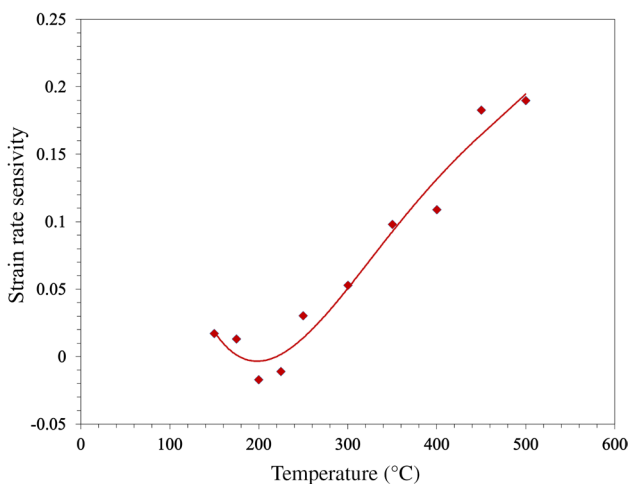


**Fig. 5** Variations of strain rate sensitivity parameter vs. temperature

optimum value was selected when the slopes of the lines in  $\ln(\dot{\epsilon})$  vs.  $\ln((\sinh(\alpha\sigma_{ss})))$  at different temperatures had the minimum variations. In other words, an approximately constant stress-exponent i.e.  $n$ -value, should be obtained. In this regard, two ranges of temperature were employed as shown in Fig. 9. The first range was selected as 250–350 °C and the other one was 350–500 °C. The values of corresponding  $n$ - and  $\alpha$ -parameter were computed as 10.3 and 0.007  $\text{MPa}^{-1}$  under lower temperatures and the values of 5.38 and 0.02  $\text{MPa}^{-1}$  were computed for the other range. In the next step, the slope in  $\ln(\dot{\epsilon})$  vs.  $T^{-1}$  coordinates at a given stress were plotted for calculating the apparent activation energy as shown in Fig. 10. Accordingly, the activation energies of 380.6  $\text{kJ mole}^{-1}$  at 250–350 °C and

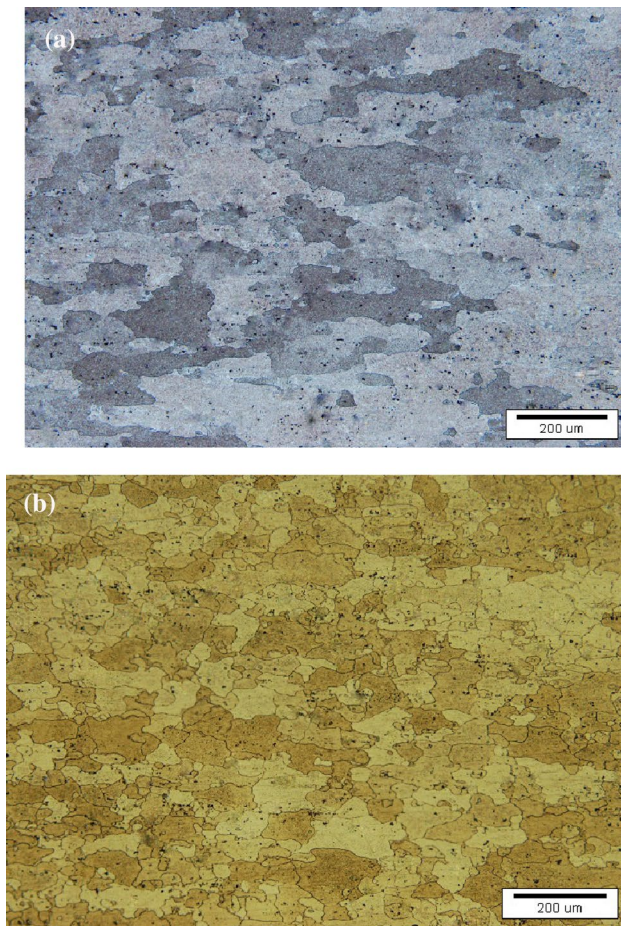


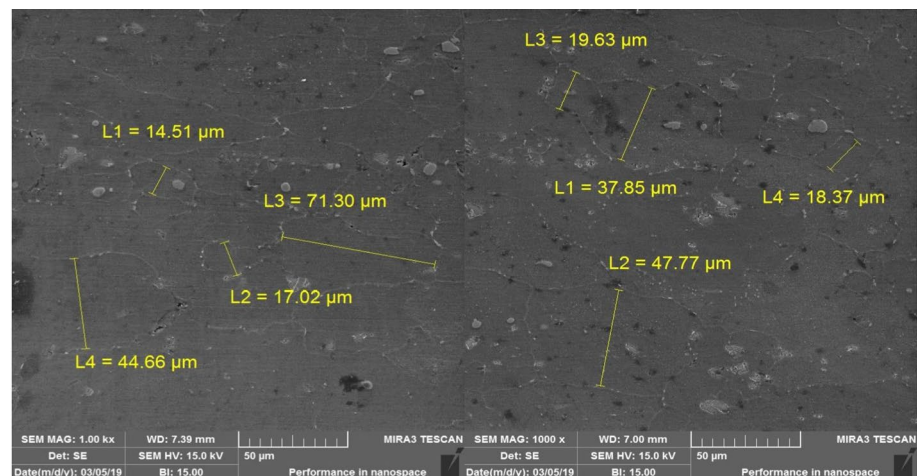
**Fig. 6** Optical images of deformed alloy, **a** at 400 °C, 0.02 s<sup>-1</sup>, **b** at 500 °C, 0.005 s<sup>-1</sup>

224.7 kJ mole<sup>-1</sup> at 350~500 °C were computed. These values illustrate that different softening mechanisms might be operative at high and low temperatures. The activation

energy of 380.6 kJ mole<sup>-1</sup> computed at 250~350 °C is much higher than the bulk self-diffusion value i.e. 142 kJ mole<sup>-1</sup>. This may be attributed to the hard particles like copper-rich precipitates and their reactions with mobile dislocations which made the softening process more difficult [22]. This leads to larger activation energies and stress exponent; however, at higher temperatures where the particles start to dissolve within the matrix, the particle-dislocation binding energy is reduced significantly and at the same time, the diffusion rate increases and thus, the softening processes including dynamic recrystallization can occur.

Two distinct neural networks were also trained for prediction of flow stress under different conditions i.e. low and high temperature ranges. The optimum network for the low temperature range had a single hidden layer containing 20 levels while the other one for the higher temperature range included two hidden layers having 10 and 15 levels. Figure 11 compares the predicted and experimental flow stress under different conditions. As seen there is a proper correlation between the two sets of data which shows the predictive capabilities of the employed neural networks. Next, the diagrams of  $\ln(\sigma)$  vs.  $\ln(\dot{\epsilon})$  at given strain and temperatures were plotted using the results of the ANN while strain rate sensitivity was determined at various strain-rates with high precision. Finally, using the calculated strain rate sensitivity parameters together with Eqs. 4–6, the processing maps were plotted. Figure 12 shows the computed processing maps of the examined alloy under different temperature ranges. In the processing map for 250~350 °C, as explained, the rate of softening mechanisms were slower and this caused the efficiency region to decrease which in turn led to a higher possibility of flow instability as shown in Fig. 12a. On the other hand, for temperatures 350~500 °C, the power dissipation

**Fig. 7** SEM image of deformed alloy at 500 °C, 0.005 s<sup>-1</sup>





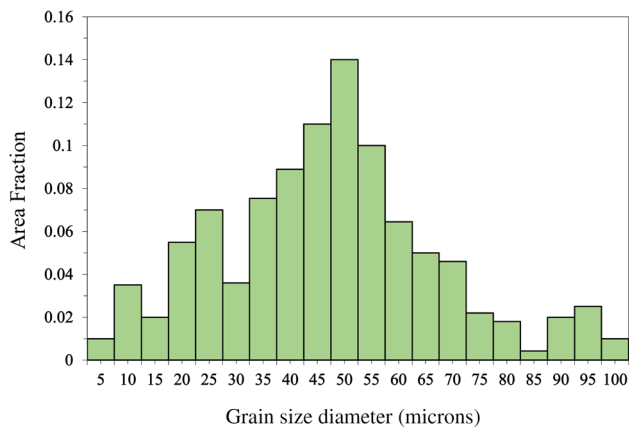


**Fig. 8** The area-weighted grain size distribution after deformation at 500 °C, 0.005 s<sup>-1</sup>

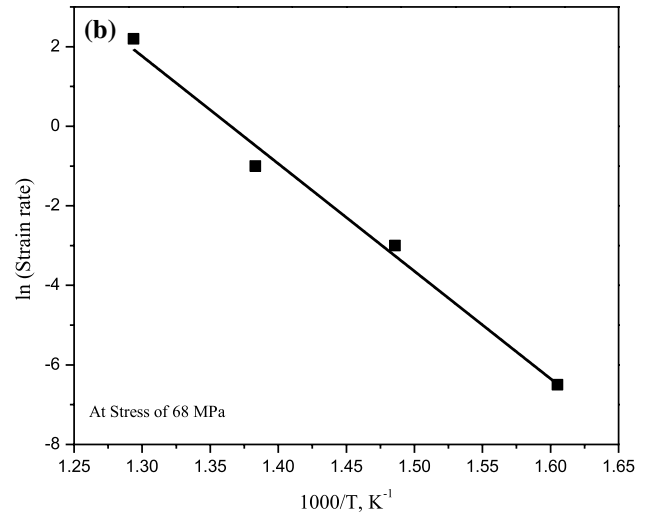
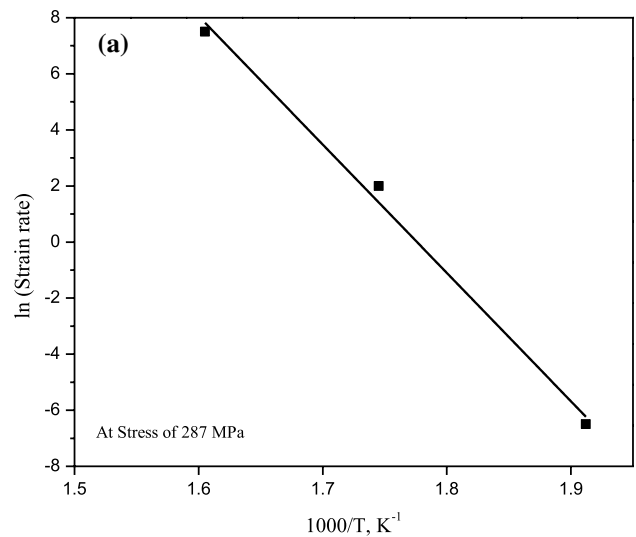


**Fig. 10** Diagram of  $\ln(\dot{\epsilon})$  vs.  $1000/T$  at given steady state stress, **a** at 250–350 °C, **b** at 350–500 °C

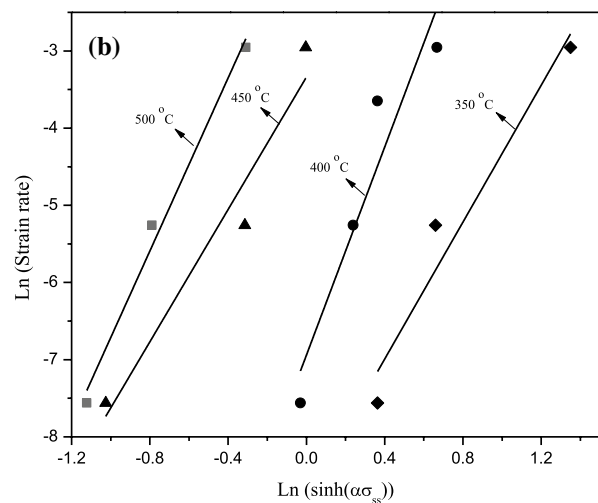
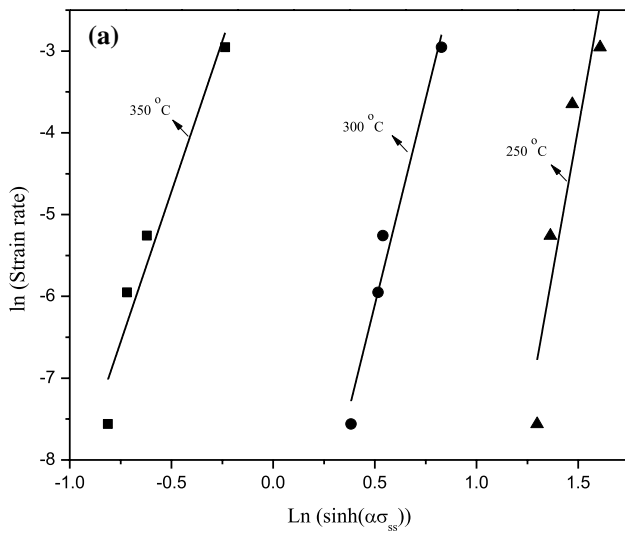


**Fig. 9** Relationship between  $\ln(\dot{\epsilon})$  with  $\ln(\sinh(\alpha\sigma_{ss}))$ , **a** at 250–350 °C, **b** 350–500 °C

efficiency increased owing to faster rate of softening and larger strain rate sensitivity parameter.

The creep behavior and cavitation were also studied. It was expected that the dislocation creep would be the dominant creep process regarding the applied stresses in the creep experiments. However, different mechanisms might be operative including viscous glide, dislocation climb and dynamic recovery, and grain boundary sliding regarding the applied stress, temperature and microstructure [13, 14]. Figure 13 displays creep behavior of the alloy at different temperatures and applied stresses. As expected an increase in the temperature or applied stress leads to higher creep rate i.e. in the secondary creep regime, however, the temperature has a stronger impact regarding this figure. Also, the rupture occurred owing to



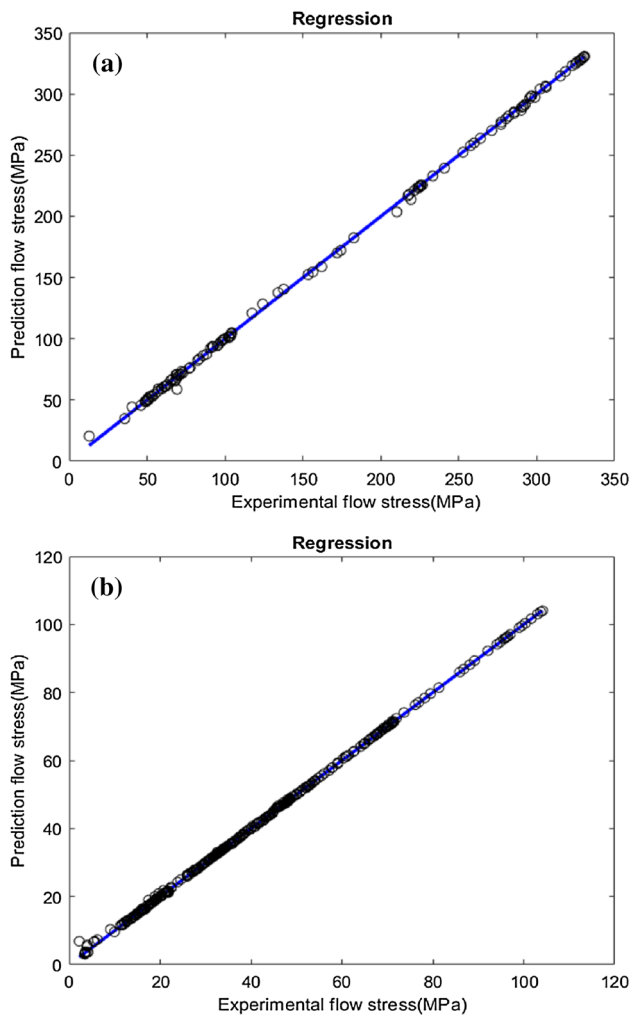


**Fig. 11** Performance of ANN model for prediction of flow stress for testing data sets in temperatures ranging, **a** 250–350 °C, **b** 350–500 °C

formation and coalescence of cavities and pseudo-brittle fracture was detected in fractured samples. The governing creep mechanism may be determined by the stress exponent and the activation energy. The creep deformation was considered as a thermally activated process and the power-law equation is mainly used to describe the constitutive equation as below [23].

$$\dot{\epsilon} = A_c \exp\left(-\frac{Q_c}{RT}\right) \sigma^{n_c} \quad (10)$$

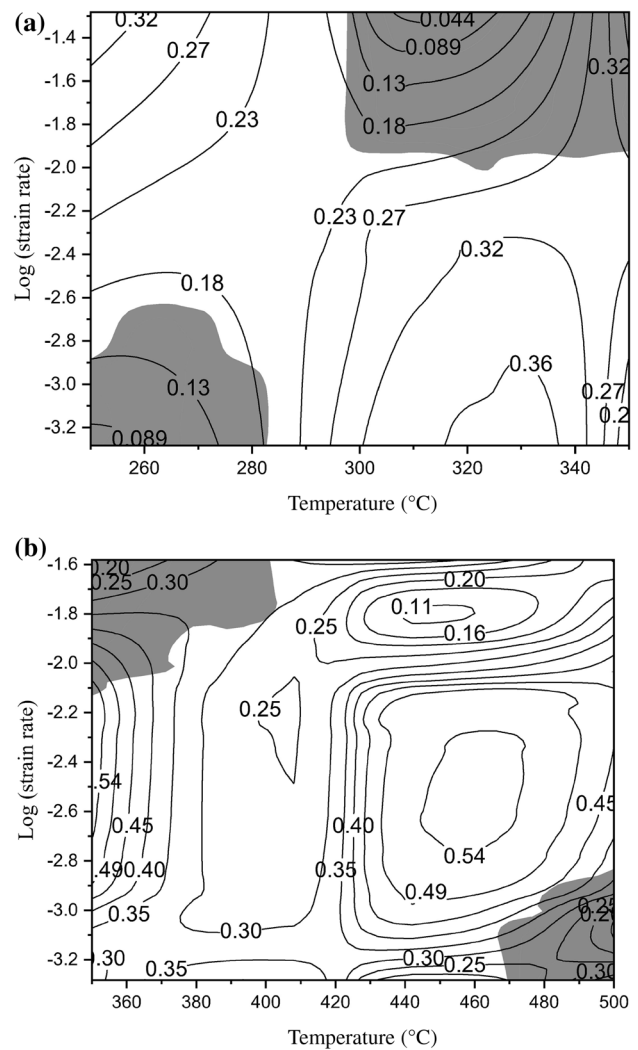


**Fig. 12** The calculated processing map, **a** at 250–350 °C, strain of 0.1, **b** at 350–500 °C, strain of 0.1

here  $A_c$ ,  $Q_c$  and  $n_c$  are material constant, creep activation energy, and stress exponent, respectively. The slope of the logarithmic diagram of the strain rate was evaluated according to Fig. 14 in order to define the stress exponent. The calculated stress exponents were in a range of 5.5 to 10.1. The changes in stress exponent denotes that the governing mechanism is changing under different conditions. The highest value was obtained at 150 °C where the copper-rich particles were still stable and accordingly the rate of dynamic recovery was lowered due to the effect of second phase particles however, at temperature of 225 °C, the coarsening and

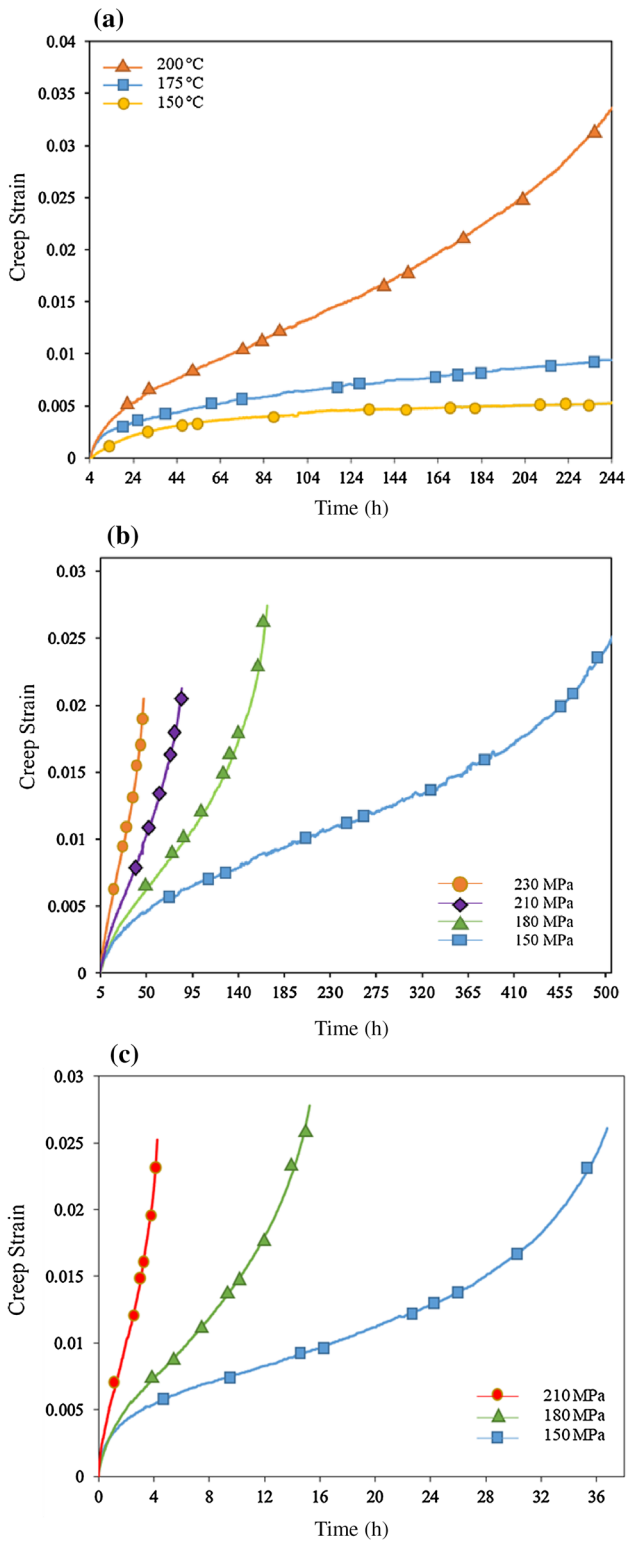


**Fig. 13** Creep diagrams at different temperatures and stresses, **a** at 210 MPa, **b** at 200 °C, **c** at 225 °C

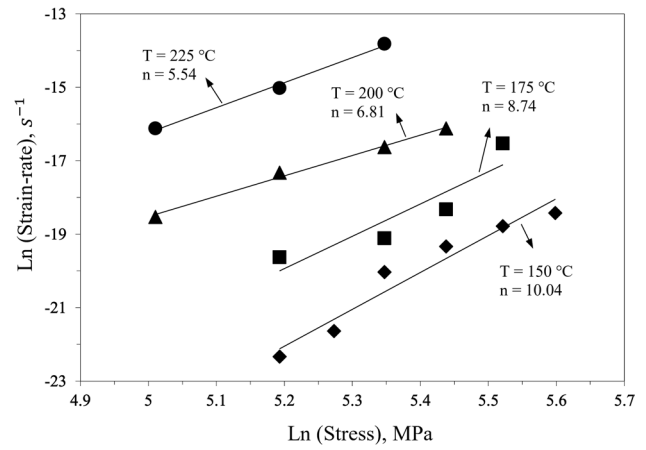


**Fig. 14** Relationship between steady-state creep rate and applied stress at different temperatures

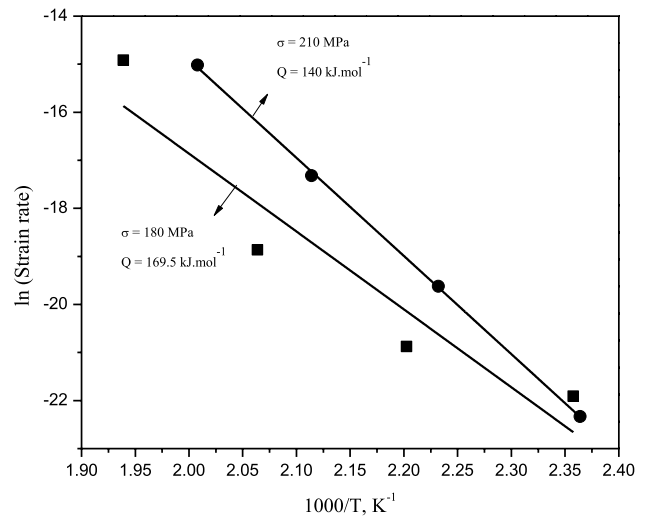
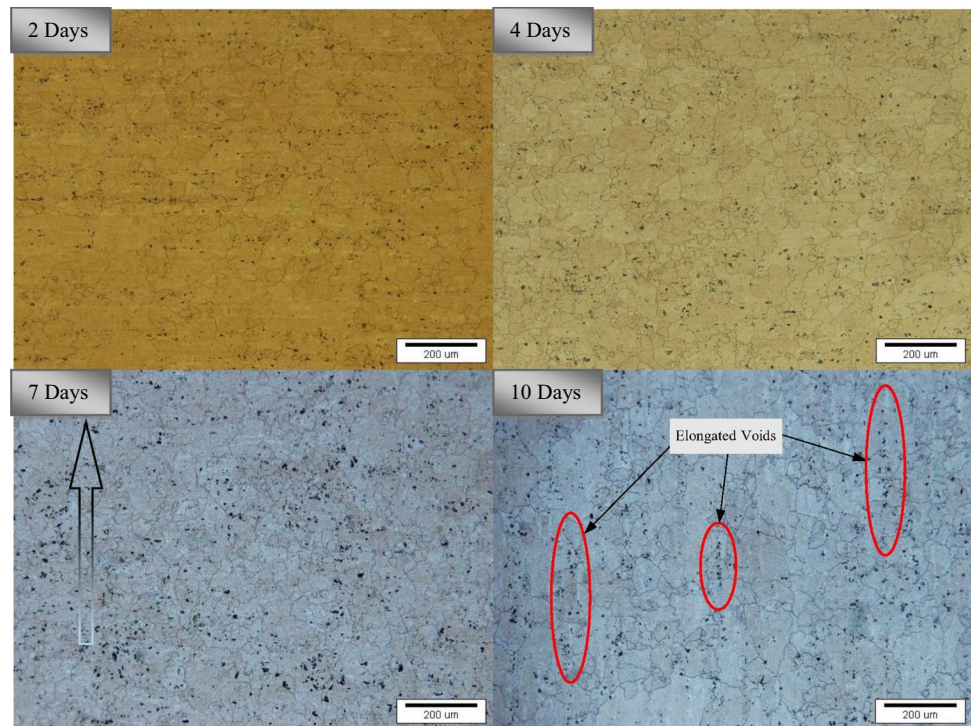


**Fig. 15** Relationship between steady creep rate and temperature

dissolving the precipitations occurred that led to faster rate of viscous glide and climb of dislocations and as a result the n-exponent was lowered to about 5 [24]. According to Eq. 10, the activation energy under the constant stress can be computed as below.

$$Q_c = -R \left( \frac{\partial(\ln(\dot{\epsilon}))}{\partial(1/T)} \right) \quad (11)$$

**Fig. 16** Microstructural changes during creep deformation at 210 MPa, 200 °C



Therefore, the activation energy was determined by plotting  $\ln(\dot{\epsilon})$  vs.  $T^{-1}$ . The activation energy of  $169.5 \text{ kJ mole}^{-1}$  was defined under applied stress of 180 MPa regarding Fig. 15. It seems that the dominant creep mechanism is the lattice diffusion-controlled dislocation climb process due to the values of stress exponent and the computed activation energy [13, 23].

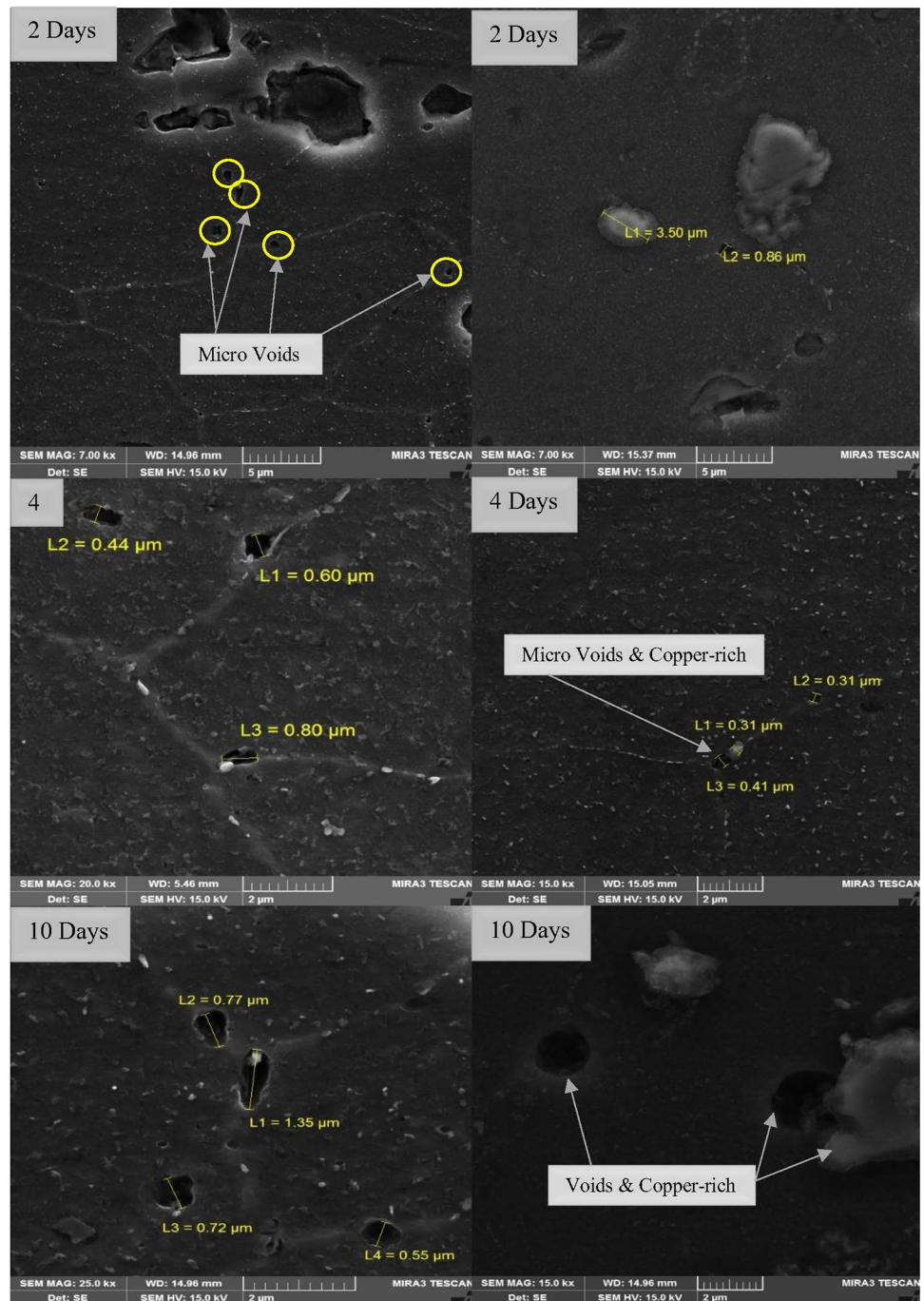
As noted earlier, cavitation in high-temperature creep is the main process leading to creep rupture especially for the materials containing hard particles such as the 2000-series aluminum alloy [25, 26]. Figure 16 shows the produced microstructure during creep deformation at 200 °C. As seen, at longer creep exposure, the cavities were increasing. Moreover, regarding the SEM-images as shown in Fig. 17, the nucleation of cavities was mainly occurred at grain boundaries as well as around the hard particles. The numbers of cavities and precipitations during creep deformation i.e. after 2, 4, 7 and 10 days, were also determined based on the microstructural observations and the results are given in Fig. 18. It should be noted that various images with different magnifications and domain areas were considered for determination of the sizes and average number of particles and cavities. To do so, "Image J" software was utilized to define the number of cavities and precipitates while at least 30 SEM images and 20 optical

images at different scales were employed for each sample. It can be observed that the precipitation number had a negative rate owing to the coarsening of particles [27]. Also, as expected both number and size of cavities were increasing during creep deformation. The cavity growth mechanism is usually divided into two main processes, the growth controlled by diffusion and controlled by the plastic straining [28]. In the early stage of growth, the governing mechanism is diffusion-controlled however, the role of strain controlled process becomes gradually important as the cavity grows larger, and after a critical cavity size, the rate controlling mechanism would be the strain-controlled process. The critical radius of cavity can be estimated by the following relationship [28].

$$\left(\frac{d\bar{r}}{d\epsilon}\right)_D = \left(\frac{d\bar{r}}{d\epsilon}\right)_s \text{ and } \bar{r}_c \approx \left(\frac{2\Omega\delta D}{RT}\right)^{1/3} \left(\frac{\sigma}{\dot{\epsilon}}\right)^{1/3} \quad (12)$$

where,  $\Omega$  is the atomic volume  $\delta$ , is the grain boundary width and/or the width of inter-phase boundary,  $D$  denotes the coefficient of diffusion at cavity/matrix interface,  $\sigma$  is the applied stress and  $\dot{\epsilon}$  is the strain rate. Using the physical data relating to the examined alloy, the critical radius was computed about  $1.3 \mu\text{m}$  for the cavities located at grain boundaries and about  $0.9 \mu\text{m}$  for the cavities formed at particle/matrix interface. After the cavity reached the critical

**Fig. 17** SEM images after creep deformation at 210 MPa, 200 °C



radius, it grew increasingly from spherical to elliptical shape which was visible at long-term exposure as displayed in

Fig. 17. Figure 18 illustrates the changes in distribution of the particle size during creep deformation, for instance the size of some particles reached 8 μm after 10 days exposure.



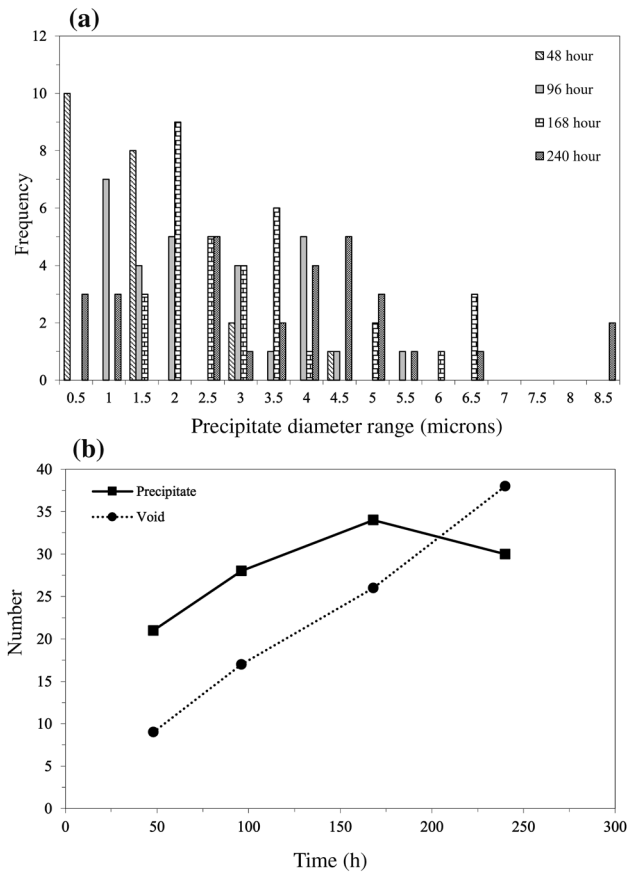


**Fig. 18** **a** Particle distribution during creep test at 200 °C, **b** number range of precipitates and voids during creep deformation at 200 °C

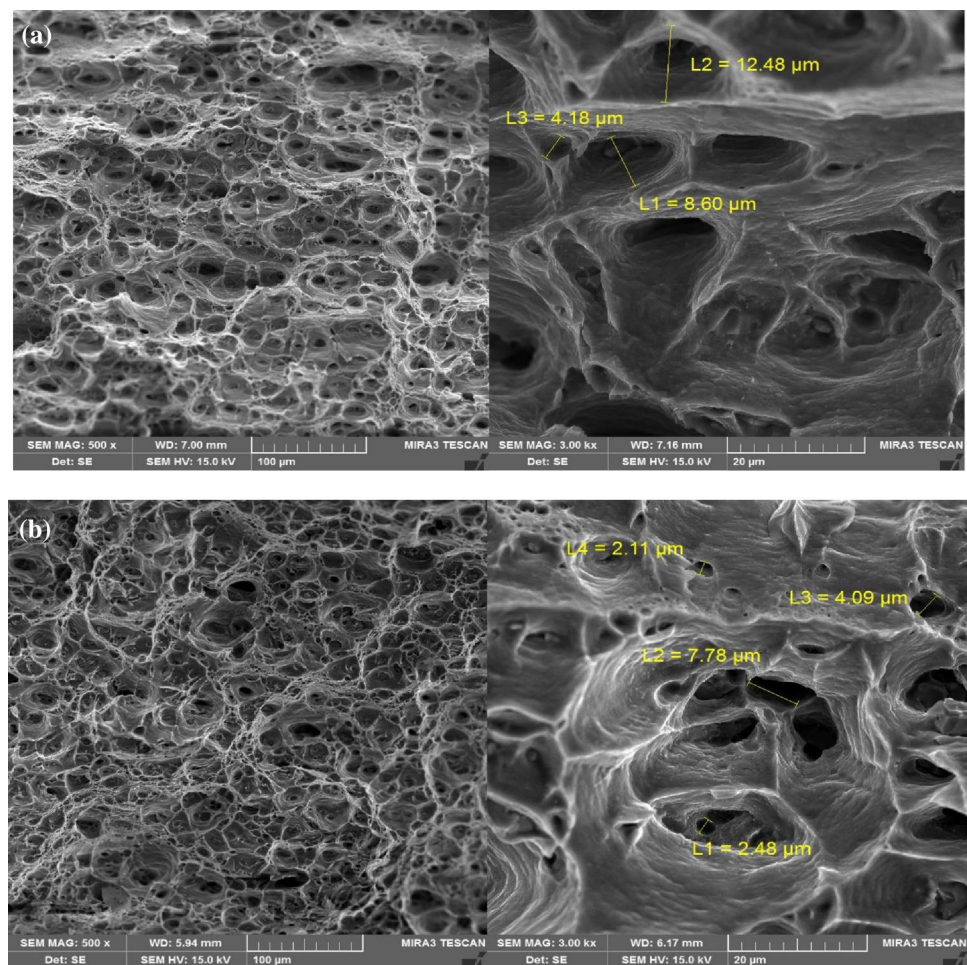
Also, the average size of the cavities i.e.  $2\bar{r}$ , reached about 1.8  $\mu\text{m}$ , 2.2  $\mu\text{m}$ , 2.9  $\mu\text{m}$  and 3.7  $\mu\text{m}$  after 2, 4, 7 and 10 days, respectively. In other words, the plastic-controlled growth of cavities was gradually dominated which eventually resulted in creep rupture due to coalescence of cavities. Two phenomena i.e. necking and cavitation can lead to fracture during creep deformation. From this perspective, it can be stated that ductile fracture or pseudo-brittle fracture can be occurred. Figure 19 shows the fractured surfaces after creep deformation under different conditions. A number of equiaxed dimples was revealed on the fracture surfaces as shown in this figure. The dimples under relatively high

temperature became more and larger as the applied stress increased. According to the size of the cavities, it may be concluded that the mode of fracture was changing from ductile to pseudo-brittle mode as the applied stress increased from 150 to 230 MPa. In fact, at the stress of 230 MPa, the cavitation had a greater impact on creep rupture.

## 4 Conclusions

The flow stress behavior of AA2017-T4 was studied using uni-axial tension tests at a relatively wide range of temperatures between 150 and 500 °C and low strain rates of 0.0005–0.05  $\text{s}^{-1}$ . Based on the results of tensile tests and neural network modeling, the flow stress behavior and strain rate sensitivity were predicted at temperatures and strain rates with small intervals of 10 °C and 0.0001  $\text{s}^{-1}$ , respectively. Then, the corresponding processing maps were defined employing dynamic material modeling. In addition, stress-controlled creep tests were performed at 150–225 °C under stresses ranging between 150 and 230 MPa. Microstructural evolutions were also carried out to detect the occurrence of dynamic recrystallization during hot deformation as well as to observe the cavitation phenomenon during creep deformation. The results indicated that dynamic precipitation occurred at temperatures 175–225 °C leading to negative strain rate sensitivity. In hot deformation range, the main softening mechanism was determined as dynamic recovery however, at the temperature of higher than 400 °C and low strain rates, dynamic recrystallization occurred. The apparent hot deformation activation energy was computed about 380.6  $\text{kJ mole}^{-1}$  at temperatures between 250 and 350 °C and 224.7  $\text{kJ mole}^{-1}$  at 350–350 °C based on hyperbolic-sine constitutive equation. The activation energy for creep deformation was computed about 169.5  $\text{kJ mole}^{-1}$  under stress of 180 MPa based on power-law equation which is found to be greater than those required for bulk diffusion of substitutional atoms in aluminum alloys. The examined alloy was prone to cavitation owing to high density of hard particles while both strain- and diffusion-controlled growth processes were activated during creep deformation.

**Fig. 19** SEM images of fracture surface after creep deformation at, **a** 150 MPa, 200 °C, **b** 230 MPa, 200 °C



## References

1. R. Carmona, Q. Zhu, C.M. Sellars, J.H. Beynon, Controlling mechanisms of deformation of AA5052 aluminium alloy at small strains under hot working conditions. *Mater. Sci. Eng. A* **393**, 157–163 (2005)
2. C.M. Cepeda-Jiménez, O.A. Ruano, M. Carsí, F. Carreño, Study of hot deformation of an Al–Cu–Mg alloy using processing maps and microstructural characterization. *Mater. Sci. Eng. A* **552**, 530–539 (2012)
3. N. Nayan, N.P. Gurao, S.V.S. Narayana Murty, A.K. Jha, B. Pant, S.C. Sharma, K.M. George, Microstructure and micro-texture evolution during large strain deformation of an aluminium–copper–lithium alloy AA 2195. *Mater. Des.* **65**, 862–868 (2015)
4. X.H. Fan, M. Li, D.Y. Li, Y.C. Shao, S.R. Zhang, Y.H. Peng, Dynamic recrystallisation and dynamic precipitation in AA6061 aluminium alloy during hot deformation. *Mater. Sci. Technol.* **30**, 1263–1272 (2014)
5. P. Cavaliere, Hot and warm forming of 2618 aluminium alloy. *Light Metals* **2**, 247–252 (2002)
6. S. Serajzadeh, S.R. Motlagh, S.M.H. Mirbagheri, J.M. Akhgar, Deformation behavior of AA2017–SiCp in warm and hot deformation regions. *Mater. Des.* **67**, 318–323 (2015)
7. S. Spigarelli, M. Cabibbo, E. Evangelist, A study of the hot formability of an Al–Cu–Mg–Zr alloy. *J. Mater. Sci.* **38**, 81–88 (2003)
8. X. Huang, H. Zhang, Y. Han, W. Wu, J. Chen, Hot deformation behavior of 2026 aluminum alloy during compression at elevated temperature. *Mater. Sci. Eng. A* **527**, 485–490 (2010)
9. H.Z. Li, H.J. Wang, X.P. Liang, H.T. Liu, Y. Liu, X.M. Zhang, Hot deformation and processing map of 2519A aluminum alloy. *Mater. Sci. Eng. A* **528**, 1548–1552 (2011)
10. J.S. Jin, X. Wang, H.E. Hu, J. Xia, High-temperature deformation behavior and processing map of 7050 aluminum alloy. *Met. Mater. Int.* **18**, 69–75 (2012)
11. X.L. Xu, L.H. Zhan, Y.G. Li, M.H. Huang, Constitutive modelling and springback prediction for creep age forming of 2124 aluminium alloy. *Mater. Sci. Technol.* **29**, 1139–1143 (2013)
12. Y.L. Yang, L.H. Zhan, X.L. Xu, Constitutive modeling for Al–Cu–Mg alloy in creep aging process. *Strength Mater.* **48**, 23–31 (2016)
13. Z.W. Du, G.J. Wang, X.L. Han, Z.H. Li, B.H. Zhu, X. Fu, Y.A. Zhang, B.Q. Xiong, Microstructural evolution after creep in aluminum alloy 2618. *J. Mater. Sci.* **47**, 2541–2547 (2012)
14. Y.C. Lin, Y.-C. Xia, Y.-Q. Jiang, H.-M. Zhou, L.-T. Li, Precipitation hardening of 2024-T3 aluminum alloy during creep aging. *Mater. Sci. Eng. A* **565**, 420–429 (2013)
15. J. Majimel, G. Molenat, M.J. Casanove, D. Schuster, A. Denquin, G. Lapasset, Investigation of the evolution of hardening precipitates during thermal exposure or creep of a 2650 aluminium alloy. *Scripta Mater.* **46**, 113–119 (2002)

16. Y. Sun, W.D. Zeng, Y.Q. Zhao, Y.L. Qi, X. Ma, Y.F. Han, Development of constitutive relationship model of Ti600 alloy using artificial neural network. *Comput. Mater. Sci.* **48**, 686–691 (2010)
17. R.M. Golden, *Mathematical Methods for Neural Network Analysis and Design* (MIT Press, Cambridge, 1996)
18. Y. Prasad, S. Sasidhara, *Hot Working Guide: A Compendium of Processing Maps* (ASM International, Cleveland, 1997)
19. M.W. Zandbergen, Q. Xu, A. Cerezo, G.D.W. Smith, Study of precipitation in Al–Mg–Si alloys by atom probe tomography I Microstructural changes as a function of ageing temperature. *Acta Materialia* **101**, 136–148 (2015)
20. L. Djapic Oosterkamp, A. Ivankovic, G. Venizelos, High strain rate properties of selected aluminium alloys. *Mater. Sci. Eng. A.* **278**, 225–235 (2000)
21. N. Jin, H. Zhang, Y. Han, W. Wu, J. Chen, Hot deformation behavior of 7150 aluminum alloy during compression at elevated temperature. *Mater. Charact.* **60**, 530–536 (2009)
22. J.G. Morris, B.J. Roopchand, The warm and hot working of dynamically strain ageable aluminum alloys. *Mater. Sci. Eng.* **17**, 77–80 (1975)
23. Y. Jiang, Y.C. Lin, C. Phaniraj, Y. Xia, H. Zhou, Creep and creep-rupture behavior of 2124-T851 aluminum alloy. *High Temp. Mater. Processes (London)* **32**, 533–540 (2013)
24. J.P. Poirier, *Creep of Crystals* (Cambridge University Press, Cambridge, 1985)
25. M.E. Kassner, T.A. Hayes, Creep cavitation in metals. *Int. J. Plast.* **19**, 1715–1748 (2003)
26. L. Li, Y.C. Lin, H. Zhou, Y. Jiang, Modeling the high-temperature creep behaviors of 7075 and 2124 aluminum alloys by continuum damage mechanics model. *Comput. Mater. Sci.* **73**, 72–78 (2013)
27. C.K.L. Davies, P. Nash, R.N. Stevens, The effect of volume fraction of precipitate on Ostwald ripening. *Acta Metall.* **28**, 179–189 (1980)
28. S. Li, S.S. Jin, Z. Huang, Cavity behavior of fine-grained 5A70 aluminum alloy during superplastic formation. *Metals* (2018). <https://doi.org/10.3390/met8121065>

**Publisher's Note** Springer Nature remains neutral with regard to jurisdictional claims in published maps and institutional affiliations.